JOURNAL OF COMPUTATIONAL PHYSICS 115, 65–85 (1994)

A Spectral Element–FCT Method for the Compressible Euler Equations

JOHN GIANNAKOUROS AND GEORGE EM KARNIADAKIS*

Center for Fluid Mechanics, Division of Applied Mathematics, Brown University, Providence, Rode Island 02912

Received October 4, 1993

A new algorithm based on spectral element discretizations and flux-corrected transport concepts is developed for the solution of the Euler equations of inviscid compressible fluid flow. A conservative formulation is proposed based on one- and two-dimensional cell-averaging and reconstruction procedures, which employ a staggered mesh of Gauss–Chebyshev and Gauss–Lobatto–Chebyshev collocation points. Particular emphasis is placed on the construction of robust boundary and interfacial conditions in one- and two-dimensions. It is demonstrated through shock-tube problems and two-dimensional simulations that the proposed algorithm leads to stable, non-oscillatory solutions of high accuracy. Of particular importance is the fact that dispersion errors are minimal, as show through experiments. From the operational point of view, casting the method in a spectral element formulation provides flexibility in the discretization, since a variable number of macro-elements or collocation points per element can be employed to accomodate both accuracy and geometric requirements.

1. INTRODUCTION

Spectral element methods are high-order weighted residual techniques for the solution of partial differential equations typically encountered in fluid dynamics [31, 20]. Their success in the recent past in simulating complex incompressible flows derives from the flexibility of the method in representing accurately non-trivial geometries while preserving the good resolution properties of spectral methods [19]. In these simulations, both the geometry and the solution are described through smooth functions so that spectral element methods can obtain exponential accuracy. This is not the case, though, for non-smooth geometries and discontinuous solutions. To address the first issue, spectral element methods for non-smooth domains have been recently developed [32]; in many situations convergence rates faster than algebraic can be recovered for the elliptic problems considered. However, the use of spectral methods in simulations with discontinuous solutions remains problematic. In particular, the success of global and multi-domain spectral methods in simulating compressible flows with shock waves has been quite limited, despite some recent significant advances (see [2–4, 8, 22, 18, 7]).

There are several issues to be addressed for a successful implementation of spectral methods to compressible flow simulations: Most importantly, devising ways to treat discontinuities in the solution (neutralizing the effects of the associated Gibbs phenomena). Also, incorporating the boundary conditions in a consistent way even in regions where either the solution or the geometry has finite regularity. This is especially important, since spectral methods in general are known to require boundary conditions that are both physically correct and computationally robust [8]. On a more fundamental level, the issue of the attainment or not of spectral accuracy in the presence of discontinuities presents another interesting question. While a problem-dependent approach may be used to address some of these issues (see, for instance, [3, 38]), it will inevitably result in loss of generality. Multi-domain spectral methods reported by Kopriva [21, 23] are very promising; however, their use of shock-fitting (as opposed to shock-capturing), along with the implicit assumption of regularity in the geometry, may somewhat limit their generality.

A straightforward application of spectral methods in flows described by discontinuous solutions is not possible as monotonicity is not preserved in high-order methods in discretizing hyperbolic conservation laws (see [12]). To demonstrate this consider, for example, the linear advection of a square wave in a periodic domain. In Fig. 1 we plot a spectral element solution based on Chebyshev collocation after 750,000 time steps ($\Delta t = 10^{-3}$). There are two important features characteristic of this spectral element simulation. First, large amplitude oscillations appear everywhere in the domain; second, the spectral element solution has been convected with the *correct speed* even after this very large number of time steps. The combination of these two

* Author to whom all correspondence should be addressed.

0021-9991/94 $6.00

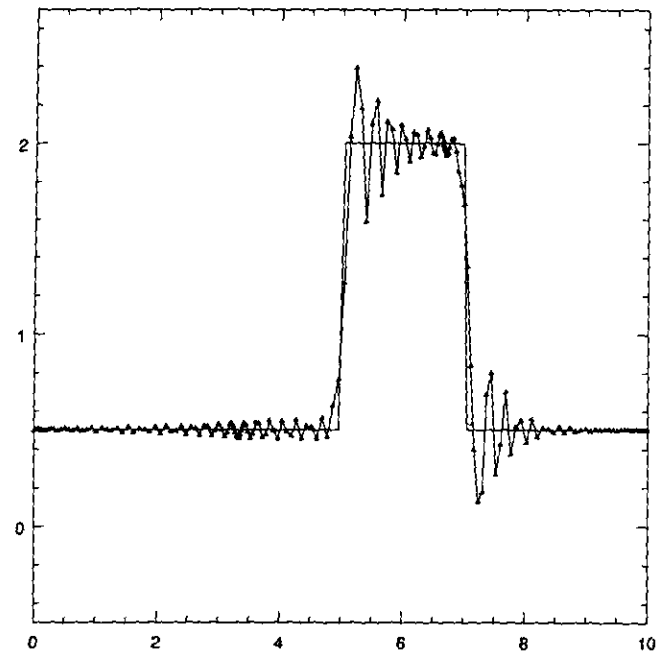

FIG. 1. Linear advection (velocity = 1) of a square wave using collocation on a spectral element discretization (three elements of equal length, 60 Chebyshev–Gauss–Lobatto points per element). Periodic boundary conditions are imposed. For the time-stepping second-order Adams–Bashforth is used. The time-integration proceeds for 750,000 time steps of size $\Delta t = 10^{-3}$; solid line, exact solution.

(seemingly contradictory) facts can only serve as numerical evidence to the argument made by Lax [25], that information is contained in these oscillations and that high-order schemes retain more information than low-order schemes.

To circumvent these difficulties a *hybrid* spectral element–FCT method was proposed in [11] for scalar hyperbolic conservation laws. This method consists of two stages, a transport or convective–diffusive stage and an antidiffusive or corrective stage. In the first stage a first-order discretization scheme is employed to preserve monotonicity, while in the second stage a multi-domain spectral algorithm is employed that corrects the intermediate solution and *dictates* the accuracy away from discontinuities. Details of the standard flux corrected transport (FCT) algorithm can be found in the original article [1] and more recent developments in [29]. The particular approach used in our work is motivated by the hybridization concepts presented in [17, 43]. In [27] McDonald has also studied the pseudospectral method as part of an FCT algorithm in solving scalar hyperbolic equations; in particular, he demonstrated through numerical experiments its superiority in accuracy regarding phase and group velocities as compared to finite difference schemes of all attainable orders (for a fixed resolution).

As in our previous work [11], the starting point is a general conservative formulation. It is based on cell averaging and reconstruction procedures that make use of a staggered one-dimensional grid of Gauss–Chebyshev and Gauss–Lobatto–Chebyshev distributions in each spectral element. Associated with the first grid are *average* quantities, while on the second grid, which includes end-points in each element, reconstructed values and fluxes are calculated. It was demonstrated in [11] for model scalar linear and non-linear problems that the spectral element–FCT algorithm leads to stable, non-oscillatory solutions of high accuracy away from discontinuities. Another important issue related to FCT algorithms has been the appearnce of terracing in smooth parts of the solution (see Fig. 2). This problem was first addressed rigorously by Grandzouan [13] who attributed the phenomenon to dispersion errors and subsequently corrected it by altering the weighting in the FCT scheme. This procedure, however, is limited to uniform meshes. Another approach in dealing with terracing effects was followed in [11], where the same assumption was made, but the approach was to minimize dispersion errors by simply resorting to an appropriate time integrator; this is explained in more detail in the current work.

In this paper, we extend the spectral element–FCT method to systems of hyperbolic conservation laws in one and two dimensions. In particular, we consider the compressible Euler equations in geometrically complex

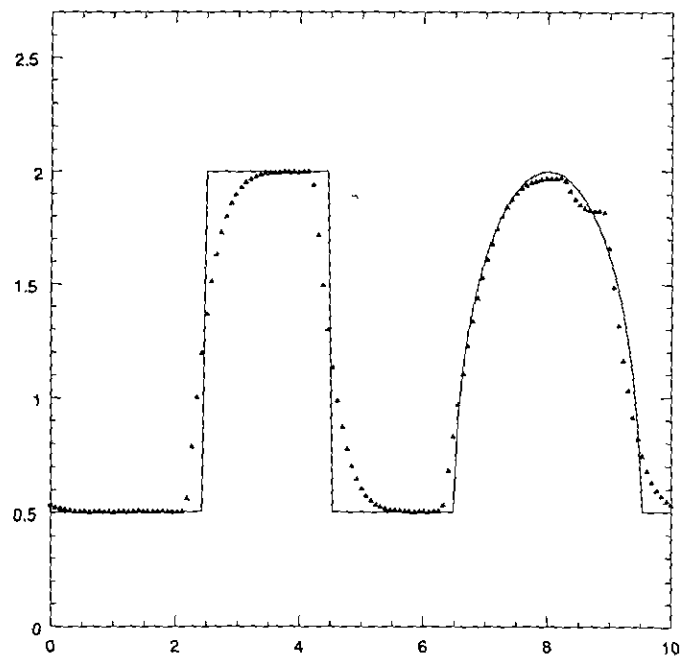

FIG. 2. Manifestation of the "terracing effect." Linear advection (velocity = 1) of a waveform consisting of a square wave and a semicircle (the axes are not drawn to the same scale). A flux-corrected transport algorithm is used, where the high-order component is formally second-order accurate. The equidistributed mesh has 128 points. Time integration: leap-frog trapezoidal. The numerical solution is plotted after 12,000 time steps ($\Delta t = 10^{-3}$).

domains. In Section 2, after presenting the one-dimensional conservative formulation we review the FCT algorithm and motivate the use of high-order schemes. In that context we define spectral element–Chebyshev cell-averaging and reconstruction procedures, and address the issue of interfacial conditions across elements. The section ends with several shock-tube results which demonstrate the accuracy of the proposed algorithm. Extensions of all these concepts to two dimensions are presented in Section 3, where we also include several benchmark problems. In Section 4, the summary preceeds a discussion on the computational efficiency of the method.

2. ONE-DIMENSIONAL FORMULATION

2.1. *Euler Equations in Conservative Form*

The system of Euler equations for polytropic gas in one dimension is given by

$$\mathbf{u}_t + \mathbf{f}(\mathbf{u})_x = 0, \tag{1a}$$

with

$$\mathbf{u} = \begin{pmatrix} \rho \\ m \\ E \end{pmatrix}, \qquad \mathbf{f} = \begin{pmatrix} m \\ m^2/\rho + P \\ (P+E)\, m/\rho \end{pmatrix}, \tag{1b}$$

$$P = (\gamma - 1)\left(E - \frac{1}{2}\frac{m^2}{\rho}\right), \tag{1c}$$

where ρ denotes density, u is velocity, P is pressure, E is total energy, $m = \rho u$ is the momentum, and γ is the ratio of the specific heats of a polytropic gas.

In the general case that we consider here the nodal points are distributed in a non-uniform manner and thus we need to define appropriate cell averaged quantities. In particular, adopting the terminology explained in Fig. 3 the cell-averaged quantity $\bar{u}_j$ is given by

$$\bar{u}_j \equiv \bar{u}(x_j, t) = \frac{1}{x_{i^+} - x_{i^-}} \int_{x_{i^-}}^{x_{i^+}} u(x, t)\, dx. \tag{4a}$$

Given this definition, the advection equation for $u(x, t)$, i.e., $\partial u/\partial x + \partial f(u)/\partial x = 0$ can be integrated along a cell extending from i^- to i^+ as

$$\frac{d\bar{u}_j}{dt} + \frac{f(u_{i^+}) - f(u_{i^-})}{\Delta x_j} = 0, \tag{2a}$$

where we have also defined

$$\Delta x_j \equiv x_{i^+} - x_{i^-}. \tag{2b}$$

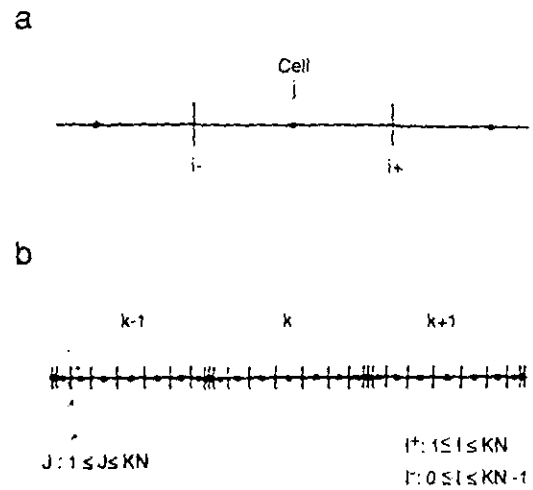

FIG. 3. Schematic for the conservative discretization: (a) The cell topology. Averaged values are stored at points j, whereas points $i^{\pm}$ contain point values. (b) Decomposition of an interval into Chebyshev spectral elements.

The above equation suggests that the fluxes $f(u)$ should be evaluated at the ends of the cell using *de-averaged* (reconstructed) velocity values; this formulation leads to the conservative (or flux) form of the semi-discrete wave equation.

2.2. *FCT Method*

The spectral element–FCT method was formulated for scalar conservation laws in [11]. Here we extend it for systems of nonlinear conservation laws. This method consists of two stages: a transport–diffusive stage and an antidiffusive or corrective stage. In the first stage, a first-order positive-type scheme is implemented, while in the second a "limited" correction due to the spectral element discretization is made.

The main steps of the proposed algorithm are as follows:

- Step 1. Evaluate the field of cell averages corresponding to the initial condition.
- Step 2. Compute the transportive fluxes corresponding to the low order scheme. The low-order positive-type scheme used here is Roe's scheme based on the cell-averaged value. The low-order flux $\mathbf{F}_{J^+}$ is defined as

$$\mathbf{F}_{J^+} = \frac{\mathbf{f}(\bar{\mathbf{u}}_{J+1}) + \mathbf{f}(\bar{\mathbf{u}}_J)}{2} - R \cdot |D| \cdot R^{-1} \frac{(\bar{\mathbf{u}}_{J+1} - \bar{\mathbf{u}}_J)}{2}, \tag{3}$$

where R is the Jacobian matrix consisting of the right-eigenvectors of the Euler system linearized around the Roe-averaged state between $\bar{\mathbf{u}}_{J+1}$ and $\bar{\mathbf{u}}_J$.

- Step 3. Advance (explicitly) cell averages in time using low-order fluxes to obtain the low order transported and

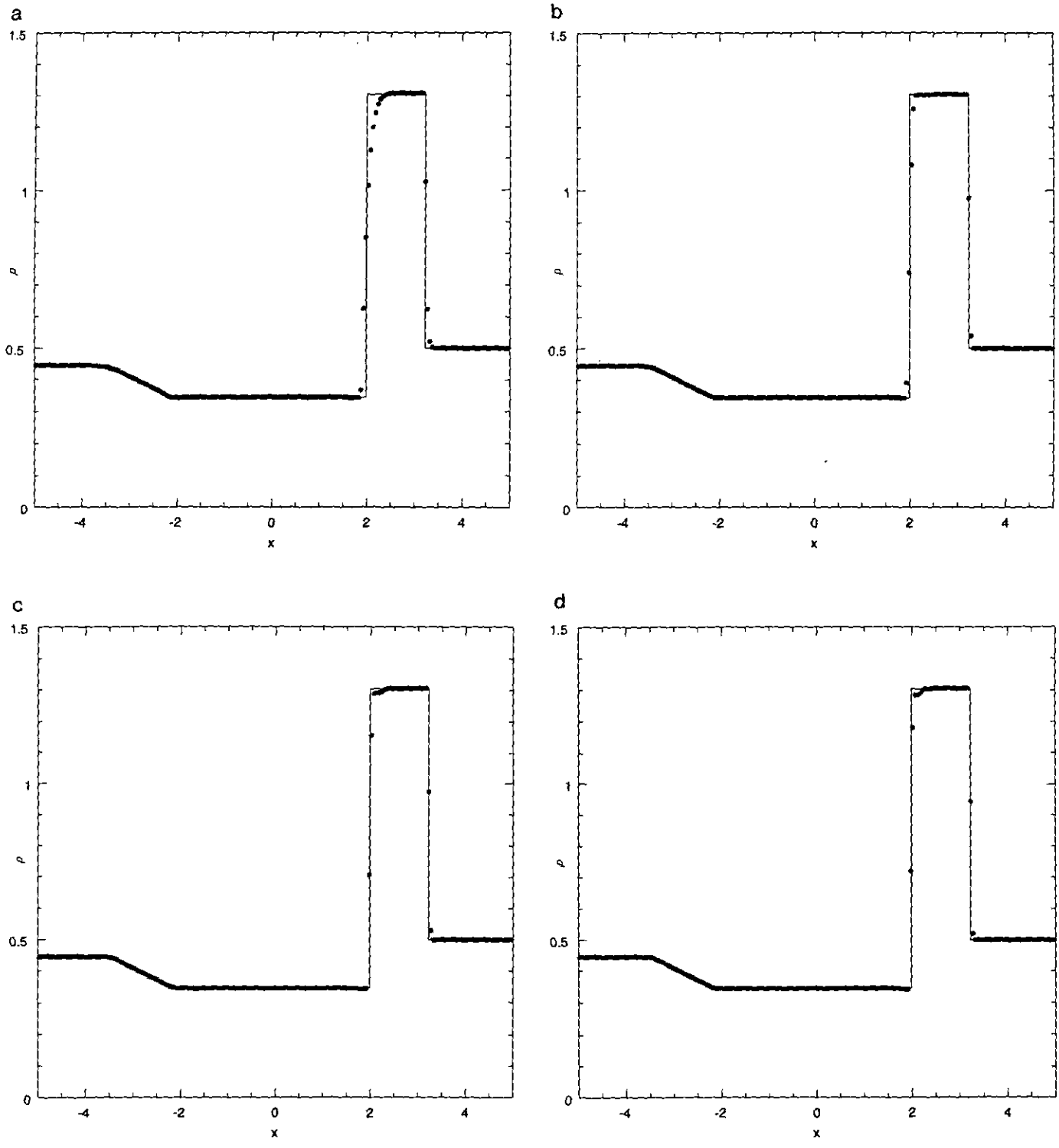

FIG. 4. Influence of the order of reconstruction on the resolution of contact discontinuities. The Lax problem is solved with a finite volume FCT method on an equidistributed mesh of 200 points. The time-stepping scheme is a hybrid between forward Euler and third-order Adams–Bashforth. Density profiles corresponding to formal orders 2, 4, 6, and 8 for the high-order scheme are plotted in a-d, respectively. The spread of the contact discontuinty varies inversely proportional with the order of reconstruction.

diffusive solution $\bar{\mathbf{u}}_j^d$. This is done using the third-order Adams–Bashforth scheme [9].

- Step 4. Compute the transportive fluxes $\mathbf{f}_I$ corresponding to the spectral element discretization.
- Step 5. Compute the antidiffusive fluxes $\mathbf{A}_I = \mathbf{f}_I - \mathbf{F}_I$ and limite them to obtain $\mathbf{A}_I^c$. Here we use the same limiter as in [11] which is based on the original ideas by Boris and Book [1] as well as the extensions presented in [27]. We found it crucial that the limiter be applied to the characteristic antidiffusive fluxes and not the componentwise fluxes.
- Step 6. Update (explicitly) the cell averages on the new time level using the limited antidiffusive fluxes (using the third-order Adams–Bashforth scheme) $\bar{\mathbf{u}}_j^{n+1}$.
- Step 7. Reconstruct point values from the cell averages at the new time level.
- Step 8. If the target time is not achieved go to Step 2.

2.3. *Representation of Discontinuities*

In his 1974 report Harten [14] argues that for discontinuities of the contact type the spread in time is proportional to the number of time-steps taken, N, to an exponent that depends on the formal order of accuracy of the spatial discretization. More precisely, if the order of scheme is r, then the spread W_T is found to be proportional to $N^{1/(r+1)}$ (some experiments to demonstrate this effect for a linear advection equation were also reported by Roe [36]). This is in contrast to the shock resolution which is independent of the number of time steps taken and depends only on the artificial viscosity of the discretization scheme. As regards the smooth part of the solution it is obvious that optimal phase properties are required. High-order schemes have proven to give excellent phase properties [27, 44] and therefore to minimize dispersion errors. In the case of the FCT algorithm, the *minmod* limiter erroneously triggered by dispersion errors may cause substantial terracing of a smooth waveform. To prevent this a high-order time-stepping can be used as proposed in [11], where a third-order Adams–Bashforth time integrator was employed for a scalar advection equation.

It is clear from the discussion above that good resolution of contact discontinuities as well as accurate representation of smooth parts of the solution require both high-order temporal and spatial discretization schemes. To demonstrate this numerically, we examine the performance of different orders of reconstruction employed as high-order schemes in the FCT context. As a model problem we choose the Lax shock-tube problem [39] solved on an equidistributed mesh. In Fig. 4 we plot the solution for a reconstruction corresponding to orders 2, 4, 6, and 8 (see also [44]) using 200 mesh points. A hybrid time-stepping consisting of a third-order Adams–Bashforth and an Euler–forward

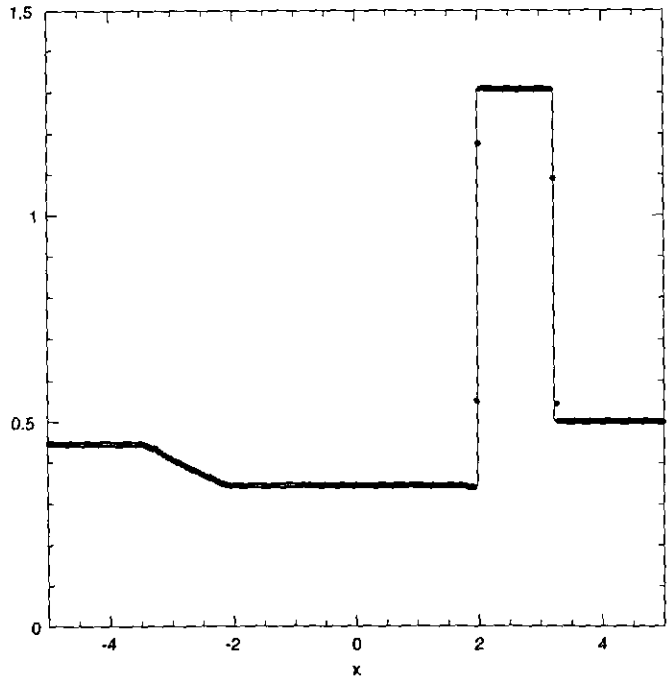

FIG. 5. Same as Fig. 4, but for Fourier high-order component. The formal order of the scheme is the highest possible for the given mesh ($N = 256$). The transition zone of the contact discontinuity is extremely narrow.

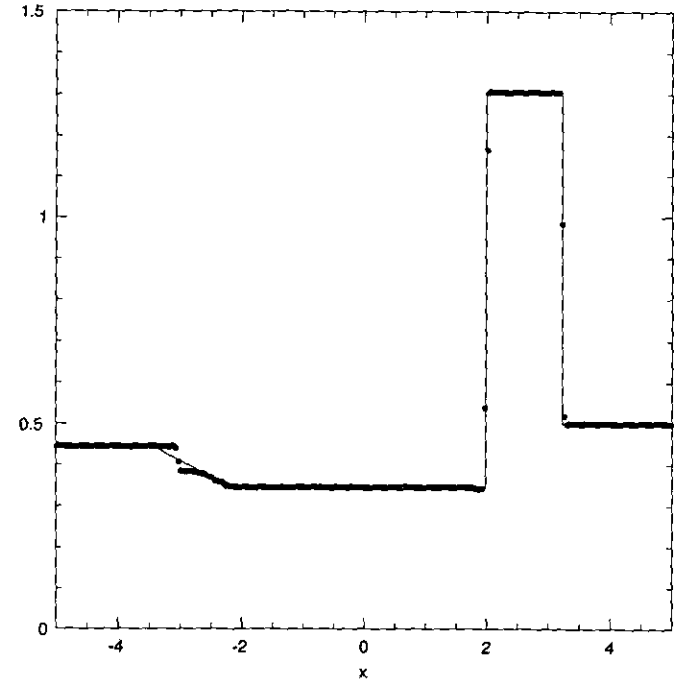

FIG. 6. Same as Fig. 5, but for simple forward Euler as time-stepping scheme. The optimal phase properties of the high-order component are damped ($N = 256$). Dramatic appearance of "terracing" in the continuous expansion region.

scheme was employed locally to advance the smooth and discontinuous part of the solution, respectively. The Adams–Bashforth scheme prevents the appearance of terracing in the expansion fan, while the resolution of contact discontinuities is improved substantially with the order of the reconstruction, in agreement with Harten's argument. These results are further improved in the limit of infinite-order (Fourier) reconstruction. This is shown in Fig. 5, where 256 modes are employed in the discretization and a hybrid time-stepping is used as before. Note that if a first-order time integration is employed throughout the domain severe terracing effects are present as shown in Fig. 6. Profiles obtained with $N = 128$ (not shown here) are also of very high quality and at least comparable to the 200 mesh points of high-order finite volume results [10].

We have also seen from the examples above the shock resolution does not depend on the order of reconstruction, consistent with the theoretical results of Harten [14]. On the other hand, the use of a high-order spatial discretization thoughout the domain does not influence the quality of the results in the shock transition zone adversely. Given these results we have chosen a Chebyshev multi-domain discretization as a high-order component in the FCT algorithm. The cell averaging and reconstruction procedures pertinent to this discretization are presented in the next section.

2.4. *Spectral Element–Chebyshev Cell Averages and Reconstruction*

A spectral–Chebyshev expansion corresponds to a non-uniform distribution of points with cells of variable size Δx_j. Following the formulation of Cai *et al.* [2] we select the set of points j to be the Gauss–Chebyshev points (see Fig. 3b) defined by

$$x_j = \cos((j - 1/2)\,\Delta\theta), \qquad \text{where} \quad \Delta\theta = \pi/N, \quad 1 \leqslant j \leqslant N \tag{4a}$$

while the end points i^+, i^- of each cell are the Gauss–Lobatto points defined as

$$x_i = \cos(i\,\Delta\theta), \qquad 0 \leqslant i \leqslant N. \tag{4b}$$

Using these two sets of points and the definition (Eqs. (4)), a Chebyshev spectral expansion of the form

$$u(x) = \sum_{k=0}^{N} a_k T_k(x), \tag{5a}$$

after averaging becomes

$$\bar{u}(x) = \sum_{k=0}^{N} a_k \bar{T}_k(x), \tag{5b}$$

where the cell averaged Chebyshev polynomial is given by

$$\bar{T}_0 = 1 \tag{6a}$$

$$\bar{T}_1 = \tfrac{1}{2}\sigma_1 U_1(x) \tag{6b}$$

$$\bar{T}_k = \tfrac{1}{2}[\sigma_k U_k(x) - \sigma_{k-2} U_{k-2}(x)], \qquad \forall k \geqslant 2, \tag{6c}$$

where

$$\sigma_k = \frac{\sin[(k+1)(\Delta\theta/2)]}{(k+1)\sin(\Delta\theta/2)}. \tag{6d}$$

Here we have introduced $U_k(x) = (1/(k+1))\,T'_{k+1}(x)$ to be the second kind of Chebyshev polynomial.

In the spectral element discretization the domain is broken up into several macro-elements (Fig. 3b) within which the velocity is expanded in terms of Chebyshev polynomials. Therefore, in the kth element an expansion of the form

$$u^k(x) = \sum_{i=0}^{N} u_i^k h_i(x) \tag{7a}$$

defined on the Gauss–Lobatto–Chebyshev points after the application of the averaging operator takes the form

$$\bar{u}^k(x) = \sum_{i=0}^{N} u_i^k \bar{h}_i(x), \tag{7b}$$

where u_i^k are the point values for element k; $h_i(x)$ and $\bar{h}_i(x)$ are the Gauss–Lobatto–Chebyshev–Lagrangian interpolant and its corresponding cell-averaged function obtained from

$$h_i(x) = \frac{2}{N} \sum_{p=0}^{N} \frac{1}{\bar{c}_i \bar{c}_p} T_p(x_i)\, T_p(x), \qquad 0 \leqslant i \leqslant N, \tag{8a}$$

$$\bar{h}_i(x) = \frac{2}{N} \sum_{p=0}^{N} \frac{1}{\bar{c}_i \bar{c}_p} T_p(x_i)\, \bar{T}_p(x), \qquad 0 \leqslant i \leqslant N, \tag{8b}$$

where $c_n = 1$ if $n \neq 0, N$ and $c_n = 2$ otherwise. In matrix form the above cell averaging procedure can be written as

$$\bar{u}_j^k = \mathbf{A}_{ji}^k \mathbf{u}_i^k, \quad 0 \leqslant i \leqslant N, \quad 0 \leqslant j \leqslant N, \tag{9}$$

where the cell averaging matrix is defined as $A_{ji}^k = \bar{h}_i(x_j)$; here x_j refers to local coordinate [31]. Based on the nodal cell averaged values obtained from (9) the corresponding polynomial can be constructed using Lagrangian interpolation, i.e.,

$$\bar{u}(x) = \sum_{j=1}^{N} \bar{u}_j^k g_j(x), \tag{10a}$$

where the Gauss–Chebyshev–Lagrangian interpolant is given by

$$g_j(x) = (-1)^{j+1} \frac{1-x_j^2}{x-x_j} \frac{T_N(x)}{N}, \qquad 1 \leqslant j \leqslant N. \quad (10b)$$

Having constructed a cell averaging procedure for the spectral element discretization we proceed next with the inverse operation of de-averaging and recovering point values for the evaluation of fluxes in Eq. (5a).

The reconstruction operation can also be put into matrix form. We consider first the polynomial describing the cell-averaged values,

$$\bar{u}(x) = \sum_{j=1}^{N} \bar{u}_j^k \, g_j(x). \quad (11a)$$

An alternative to (10b) expression for the Gauss–Chebyshev–Lagrangian interpolant is

$$g_j(x) = \sum_{p=0}^{N-1} \frac{2}{N\bar{c}_p} T_p(x_j) \, T_p(x). \quad (11b)$$

We can also express the $g_j(x)$ in terms of the second kind Chebyshev polynomials; to this end we recall that

$$T_p(x) = \tfrac{1}{2}[\, U_p(x) - U_{p-2}(x)\,], \qquad \forall p \geqslant 2. \quad (12a)$$

Using the above equation we can rewrite $g_j(x)$ as

$$g_j(x) = \sum_{p=0}^{N-1} \lambda_p^j \sigma_p \, U_p(x), \qquad 1 \leqslant j \leqslant N. \quad (12b)$$

Here we have defined:

$$\lambda_p^j = \frac{1}{N} T_p(x_j) \qquad \text{for} \quad p = N-2, N-1, \quad (12c)$$

$$\lambda_p^j = \frac{1}{N} [\, T_p(x_j) - T_{p+2}(x_j)\,] \qquad \text{for} \quad 0 \leqslant p \leqslant N-3. \quad (12d)$$

The interpolating polynomial corresponding to point values (Gauss–Chebyshev–Lobatto points) can then be constructed using the *de-averaged* Lagrangian interpolants G_j as

$$u(x) = \sum_{j=1}^{N} \bar{u}_j^j G_j(x). \quad (13)$$

The cell-averaged second kind Chebyshev polynomial is obtained using the definition of Eq. (4) (see details in [2]),

$$\bar{U}_p(x) = \sigma_p \, U_p(x) \quad (14)$$

with σ_p obtained from Eq. (6d). To determine $G_j(x)$ therefore we consider (13)–(14) and (12) and thus we obtain

$$G_j(x) = \sum_{p=0}^{N-1} \frac{\lambda_p^j}{\sigma_p} U_p(x). \quad (15)$$

To recover the point values u_i we simply set $x = x_i$ in the interpolating polynomial $u(x)$. In matrix form the reconstruction procedure (on elemental level) can be written in the form

$$\mathbf{u}_i = \mathbf{g}_{ij}^* \bar{u}_j \qquad \text{for} \quad 1 \leqslant j \leqslant N, \quad 1 \leqslant i \leqslant N, \quad (16a)$$

where

$$g_{ij}^* = G_j(x_i). \quad (16b)$$

Based on these N point values the interpolating polynomial $u(x)$ can then be constructed from Eq. (13). This local reconstruction procedure is repeated for all elements. To form a global interpolant, however, we need to impose continuity conditions at elemental interfaces as we explain in the next section.

2.5. *Boundary and Interfacial Conditions*

While the discretization of the Euler system using the cell-averaging approach is straightforward, the imposition of the interfacial condition requires further discussion. A method for imposing characteristic boundary conditions on the conservative variables is presented in [8]. The interfacial condition can be imposed in a similar way; however, the reconstructed values are needed for the computation of the numerical fluxes. It is therefore more efficient to impose boundary and interfacial conditions on the numerical fluxes directly [38]. To do so, we consider the (reconstructed) conservative variables defined at the same point but on different elements to be the left and right states of af one-dimensional Riemann problem, in much the same way as flux-point values are treated in MUSCL schemes [26]. In detail the procedure is as follows:

Consider the Jacobian matrix of the system given in Eq. (1) by $A(\mathbf{u}) = \partial \mathbf{f}/\partial \mathbf{u}$. The right-eigenvectors of A are

$$\mathbf{r}_1(\mathbf{u}) = \begin{pmatrix} 1 \\ u-c \\ H-uc \end{pmatrix}, \quad \mathbf{r}_2(\mathbf{u}) = \begin{pmatrix} 1 \\ u \\ \frac{1}{2}u^2 \end{pmatrix}, \quad \mathbf{r}_3(\mathbf{u}) = \begin{pmatrix} 1 \\ u+c \\ H+uc \end{pmatrix}, \quad (17)$$

where $c = \sqrt{\gamma P/\rho}$ is the speed of sound and the enthalpy H is defined by

$$H = \frac{(E+P)}{\rho} = \frac{c^2}{\gamma - 1} + \frac{1}{2}u^2. \quad (18)$$

Let us denote the matrix of right-eigenvectors of the Jacobian $A = A(\tilde{\mathbf{u}})$ as

$$R = (\mathbf{r}_1(\tilde{\mathbf{u}}), \mathbf{r}_2(\tilde{\mathbf{u}}), \mathbf{r}_3(\tilde{\mathbf{u}})), \tag{19}$$

where $\tilde{\mathbf{u}}$ is the Roe-averaged state (see [35]) between the states $\mathbf{u}_N^e$ and $\mathbf{u}_0^{e+1}$ at the ends of two adjacent elements e, $(e+1)$. Here N and 0 denote the rightmost and the leftmost elemental nodes, respectively. Then

$$D \equiv R^{-1} \cdot A \cdot R = \begin{pmatrix} \lambda_1 & 0 & 0 \\ 0 & \lambda_2 & 0 \\ 0 & 0 & \lambda_3 \end{pmatrix}, \tag{20}$$

where the eigenvalues of A are given by

$$\lambda_1 = u - c, \qquad \lambda_2 = u, \qquad \lambda_3 = u + c. \tag{21}$$

The flux to be imposed at the interface γ between elements e and $(e+1)$ is determined by Roe's flux-splitting (see [35]) as:

$$\mathbf{f}_\gamma = \frac{\mathbf{f}(\mathbf{u}_0^{e+1}) + \mathbf{f}(\mathbf{u}_N^e)}{2} - R \cdot |D| \cdot R^{-1} \frac{(\mathbf{u}_0^{e+1} - \mathbf{u}_N^e)}{2}. \tag{22}$$

Other choices are also possible (e.g., [30, 16]).

In the case of boundary conditions a similar procedure is

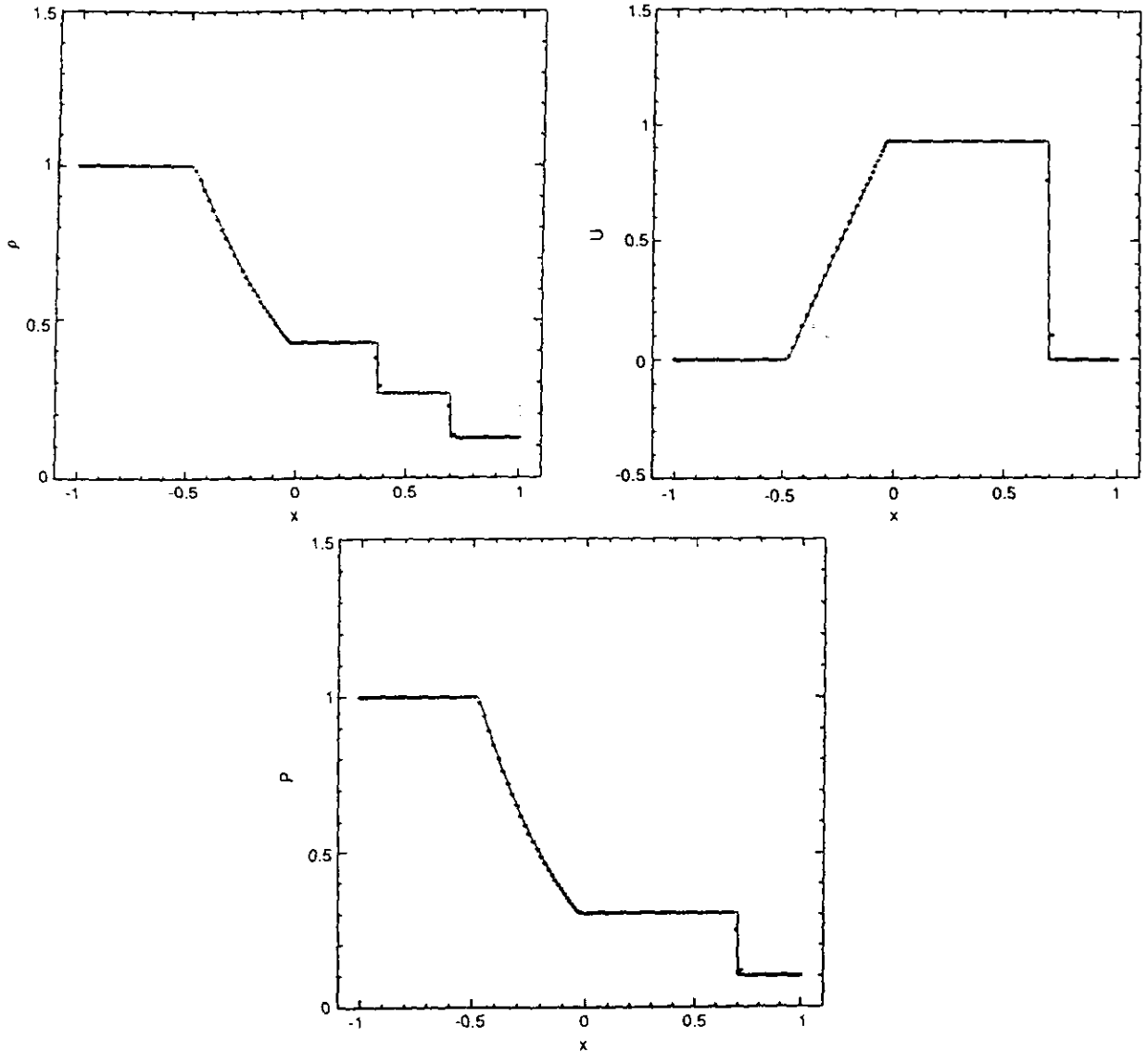

FIG. 7. Spectral element-FCT method. Solution of the Sod Riemann problem with $K = 2$, $N = 75$ at time $t = 0.4$. Profiles for density, velocity, pressure (the solid line represents the exact solution). Note the narrowness of the moving contact discontinuity in the density profile as well as the faithful representation of corners in all profiles.

followed by assuming a fictitious spectral element where either an extrapolation is made from the domain interior as in supersonic outflow or the known variables are stored as inflow and subsonic outflow. The effect of walls is reproduced by creating fictitious cells where the variables are mirrored from inside the domain (both the averages and the reconstructed).

2.6. *Numerical Results*

We begin by demonstrating the output of our algorithm for two well-known benchmark test cases, namely the so-called Sod and Lax shock tube problems. In both cases, a single diaphragm separates initially two phases of the same gas. They are defined by the following initial data [39]:

1. Sod's problem

$$\begin{aligned} &\rho_l = 1, \quad q_l = 0, \quad P_l = 1, \quad -1 \leqslant x \leqslant 0, \\ &\rho_r = 0.125, \quad q_r = 0, \quad P_r = 0.1, \quad 0 \leqslant x \leqslant 1, \end{aligned} \tag{23}$$

2. Lax's problem:

$$\begin{aligned} &\rho_l = 0.445, \quad q_l = 0.698, \quad P_l = 3.528, \quad -1 \leqslant x \leqslant 0, \\ &\rho_r = 0{,}5, \quad q_r = 0, \quad P_r = 0.571, \quad 0 \leqslant x \leqslant 1. \end{aligned} \tag{24}$$

In Fig. 7 we plot the solution to the Sod problem corresponding to $K = 2$ spectral elements (of the same length) with $N = 75$ Gauss–Lobatto–Chebyshev points in each,

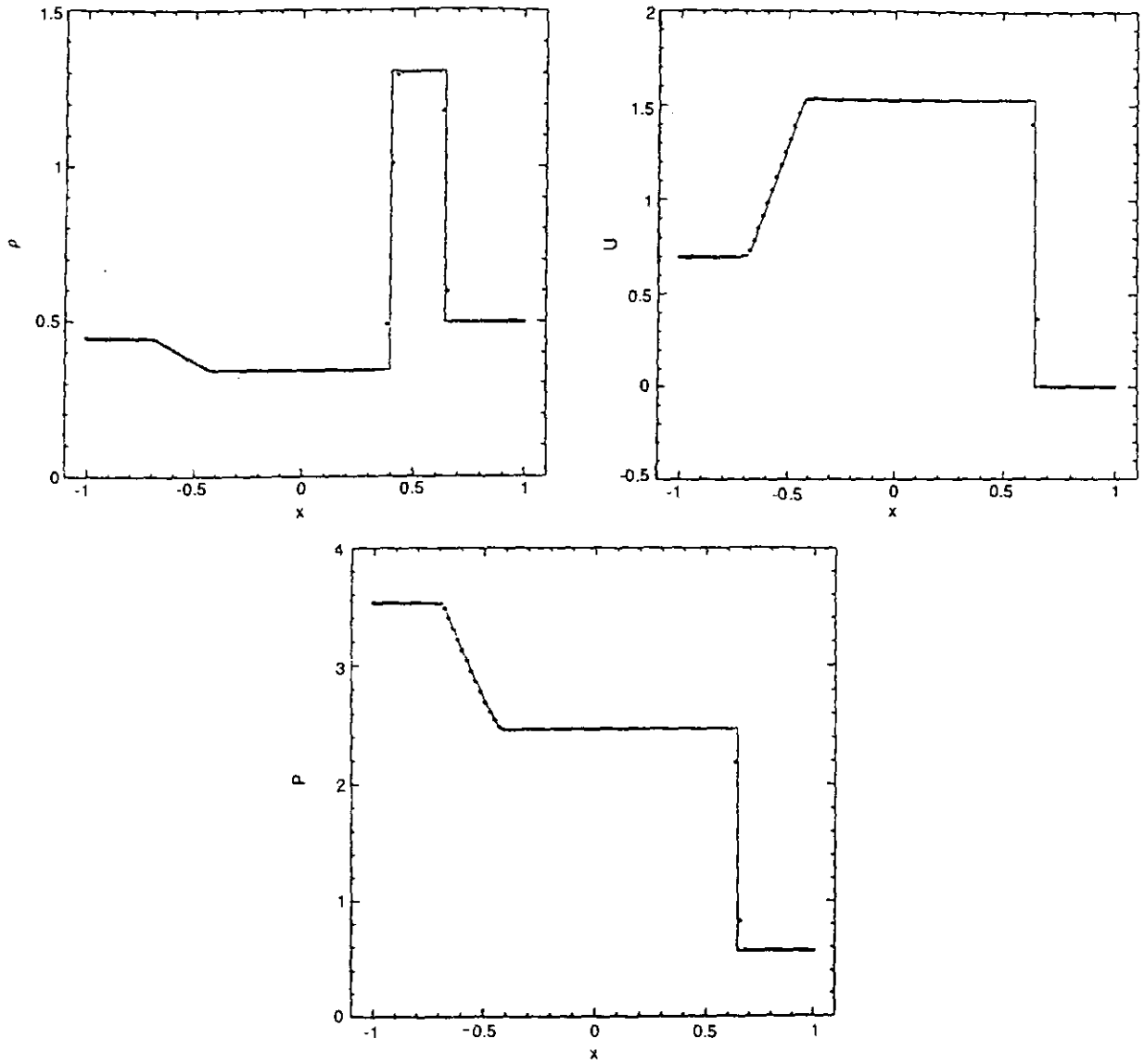

FIG. 8. Spectral element-FCT method. Solution of the Lax Riemann problem with $K = 2$, $N = 75$ at time $t = 0.26$. Profiles for density, velocity, pressure (the solid line represents the exact solution). The same observations apply as for Fig. 7.

at time $t = 0.4$. The agreement with the exact solution represented by the solid line is very good; in particular, both the contact discontinuity and the shock are two-point transitions while the end-points of the rarefaction fan preserve their sharpness.

For the Lax problem the solution is shown in Fig. 8 for the same discretization at time $t = 0.26$. The same observations regarding accuracy apply here; the contact discontinuity is captured with three points. Experiments with a different discretization consisting of $K = 75$ and $N = 3$ (corresponding to the same total number of grid points as in Fig. 8) show less sharp profiles, as seen in Fig. 9. The contact discontinuity is now a 10 point-transition which, along with the results of Fig. 8 suggest that high-order polynomial approximation does indeed result in sharp resolution of contact discontinuities, in agreement with Harten's [14] theoretical postulates (see Section 2.3). Also, the ends of the expansion fan have been smeared significantly in the low-order polynomial approximation.

In order to investigate the effect of different discretizations as defined by the pair (K, N), we have performed several experiments for the aforementioned benchmark problems. Our results have shown consistently the same influence of high-order approximation to the quality of contact discontinuities and rerefaction fans. However, for certain discretizations the appearnce of localized errors was observed. One such situation involes the Lax problem solved on a mesh consisting of $K = 10$ and $N = 16$ and producing the pressure profile plotted in Fig. 10. It is seen that there has occurred an accumulation of errors concentrated at and around elemental boundaries where the shock has crossed. At the same time, solving for the Sod problem

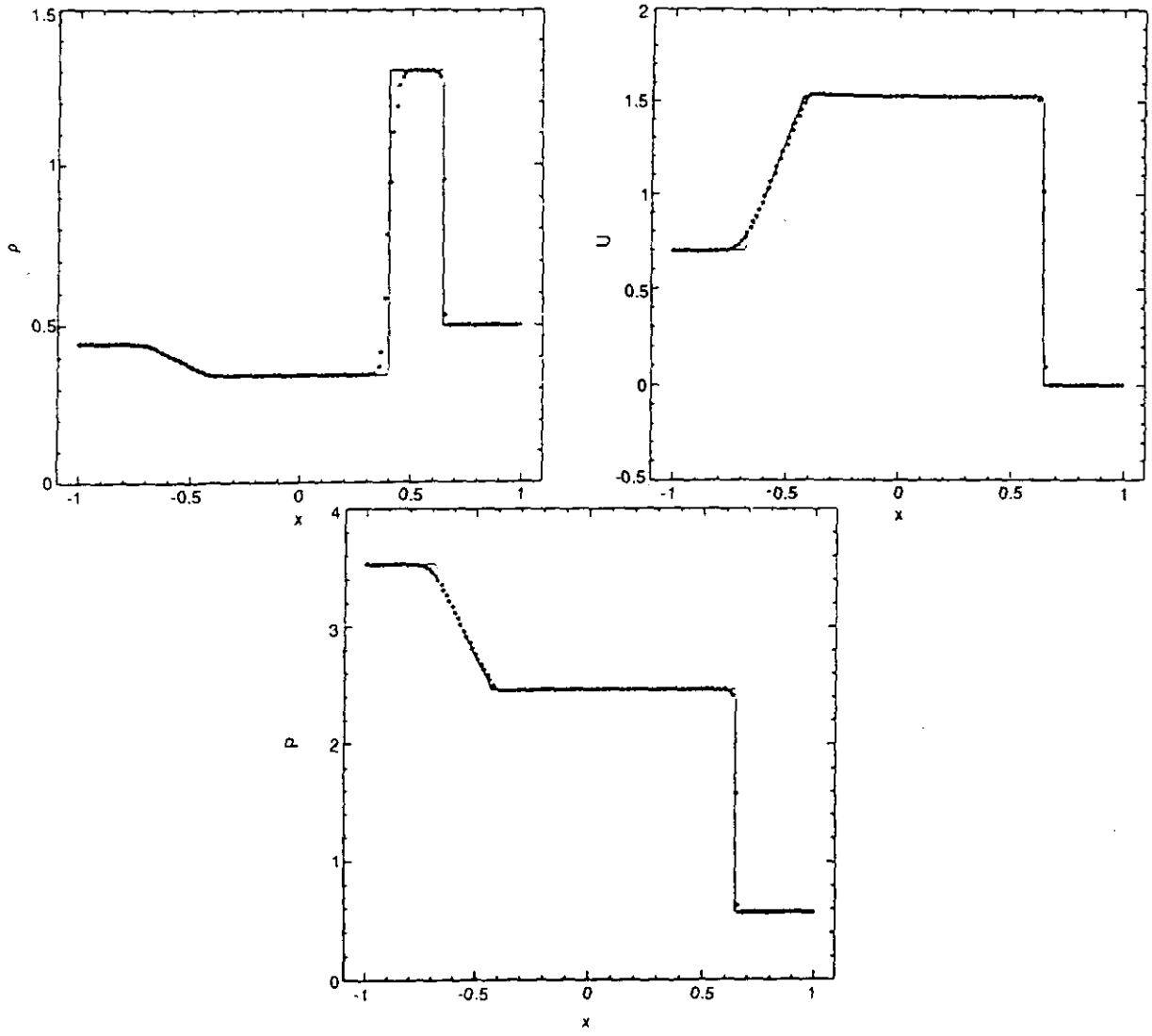

FIG. 9. Same as Fig. 8. Solution of the Lax Riemann problem at time $t = 0.26$, now with $K = 50$, $N = 3$. Profiles for density, velocity, pressure. We have lower formal order of accuracy than previously, thus we expect inferior phase properties. The quality of the results has decreased.

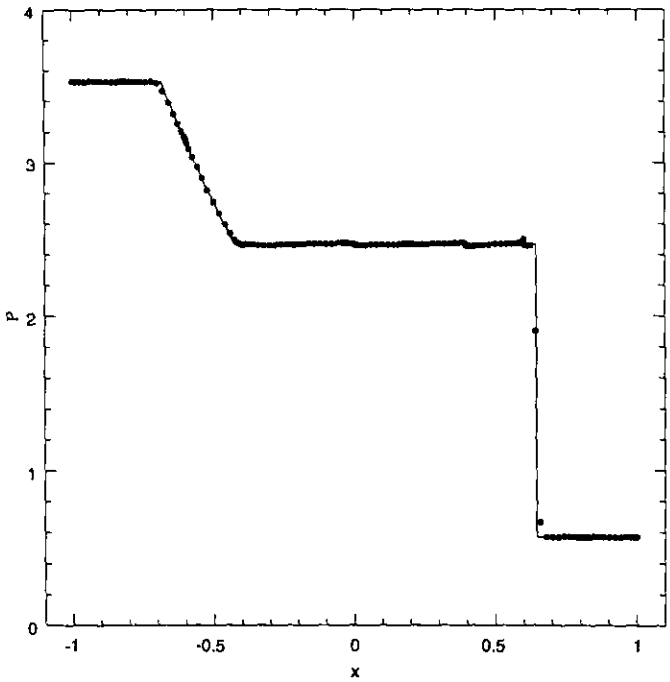

FIG. 10. Spectral element-FCT method. Solution of the Lax Riemann problem with $K = 10$, $N = 16$ at time $t = 0.26$. Profile for pressure. The low-order scheme is affected by the strongly varying Chebyshev mesh. "Kinks" are generated whenever the shock crosses an element boundary.

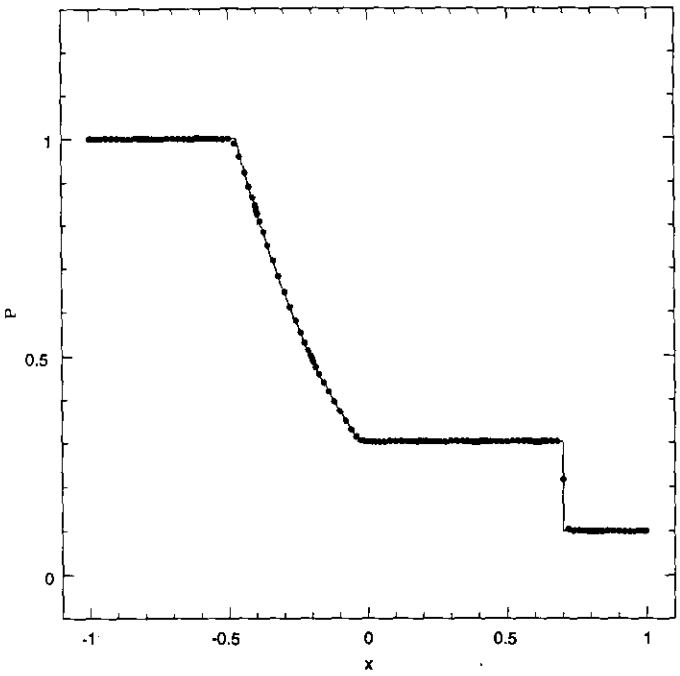

FIG. 11. Spectral element-FCT method. Solution of the Sod Riemann problem with $K = 10$, $N = 16$ at time $t = 0.40$. The shock now is less strong than that of the Lax problem. The pressure profile is unaffected.

on the same mesh produces the pressure distribution shown in Fig. 11, is free of the aformentioned problem. Having observed that the appearance of large errors is connected with the passage of shocks through elemental boundaries, we performed an analysis with the following model problem to investigate this phenomenon more systematically.

The general solution to a Riemann problem consists of at most three distinct regions in space/time (where the conservative variables keep the same values throughout), separated by a combination of at most three transition zones, i.e., shocks, contact discontinuities, and rarefaction fans. However, it is possible to obtain a solution consisting of two regions in space/time separated by a single shock wave. Derivation of such solutions is presented, e.g., in [10]. This allows us to isolate the combined effect of shock strength and discretization on the quality of the solution. The model problem we have considered corresponds to a two-phase shock tube configuration. Only the left state needs to be specified ($\rho = 1$; $u = 1$), while the quantities on the right are determined by the requirement that the flow there is initially at rest and that the two states lie on the same two-shock curve in state space [40]. We take the control parameter in these experiments to be the Mach number of the left state (M_L) with respect to a stationary reference frame (this also defines the left pressure for constant γ; we take $\gamma = 1.4$). We note that the high values of M_L cause large strength of the resulting shock. To more closely characterize this dependence we introduce the Mach number of the right state with respect to the reference frame of the moving shock (M_R^s). It is shown in [10] that there is a limiting value of $M_L = 1.8898$ past which the Riemann problem does not have a single shock solution. It is also shown that as this limit is approached the corresponding M_R^s tends to infinity.

In Figs. 12 and 13 we show results for two different discretizations and three different values of M_L corresponding to increasing strength of the resulting shock. The two discretizations considered here correspond to a multiple-domain ($K = 10$, $N = 11$; Fig. 12) and a mono-domain case ($K = 1$, $N = 101$; Fig. 13). The domain extends from -5 to $+5$ and the shock is initially located at $x = -4$. Final states are plotted with the shock having arrived at $x = 4$. We see that in both discretizations, post-shock oscillations are produced above a threshold value for M_L; in the mono-domain case these oscillations are weaker and the shock is represented as a two-point transition. Examination of the corresponding velocity profile (not shown here) even for the high M_L cases shown no oscillations at all. The reason that oscillations are produced is due to the rapid clustering of collocation points, which in this case is more severe for the rapid clustering of collocation points, which in this case is more severe for the multi-domain example as the shock crosses regions of rapid contraction/expansion many times. In the mono-domain case the spacing in the interior of the domain varies slowly and is proportional to $1/N$, in contrast

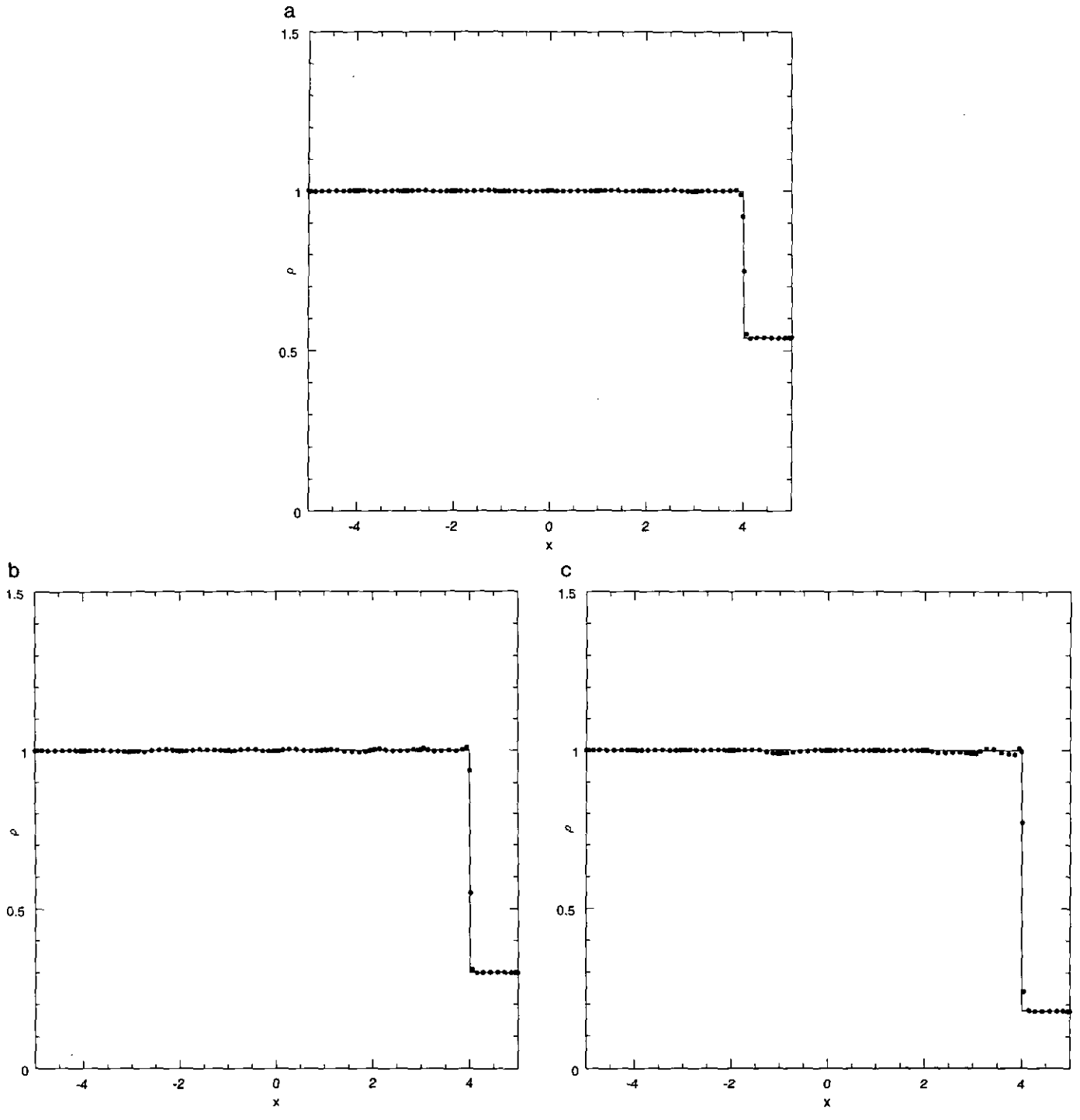

FIG. 12. Spectral element-FCT method. A shock tube problem with a single-shock solution. Combined effect of the shock strength and of the changing scale of the Chebyshev mesh on the quality of the density profile. Discretizaion: $K = 10$, $N = 11$. Mach number of the left state in the laboratory frame: (a) 0.6; (b) 1.2; (c) 1.8. The shock strength increases with this Mach number.

to the ends of the domain where it scales as $1/N^2$. The problem of post-shock oscillations is typical of shock-capturing schemes on nonuniform meshes with superlinear clustering or expansion of collocation points (flux points). Indeed experiments with an ENO scheme on a mesh similar to the ones presented here gave similar results [37]. It is not entirely clear how to characterize a strong shock but the work in [10] suggests that in this particular case it is the value of M_R^s that most closely provides such a classification. For example, following that analysis we find that the shock

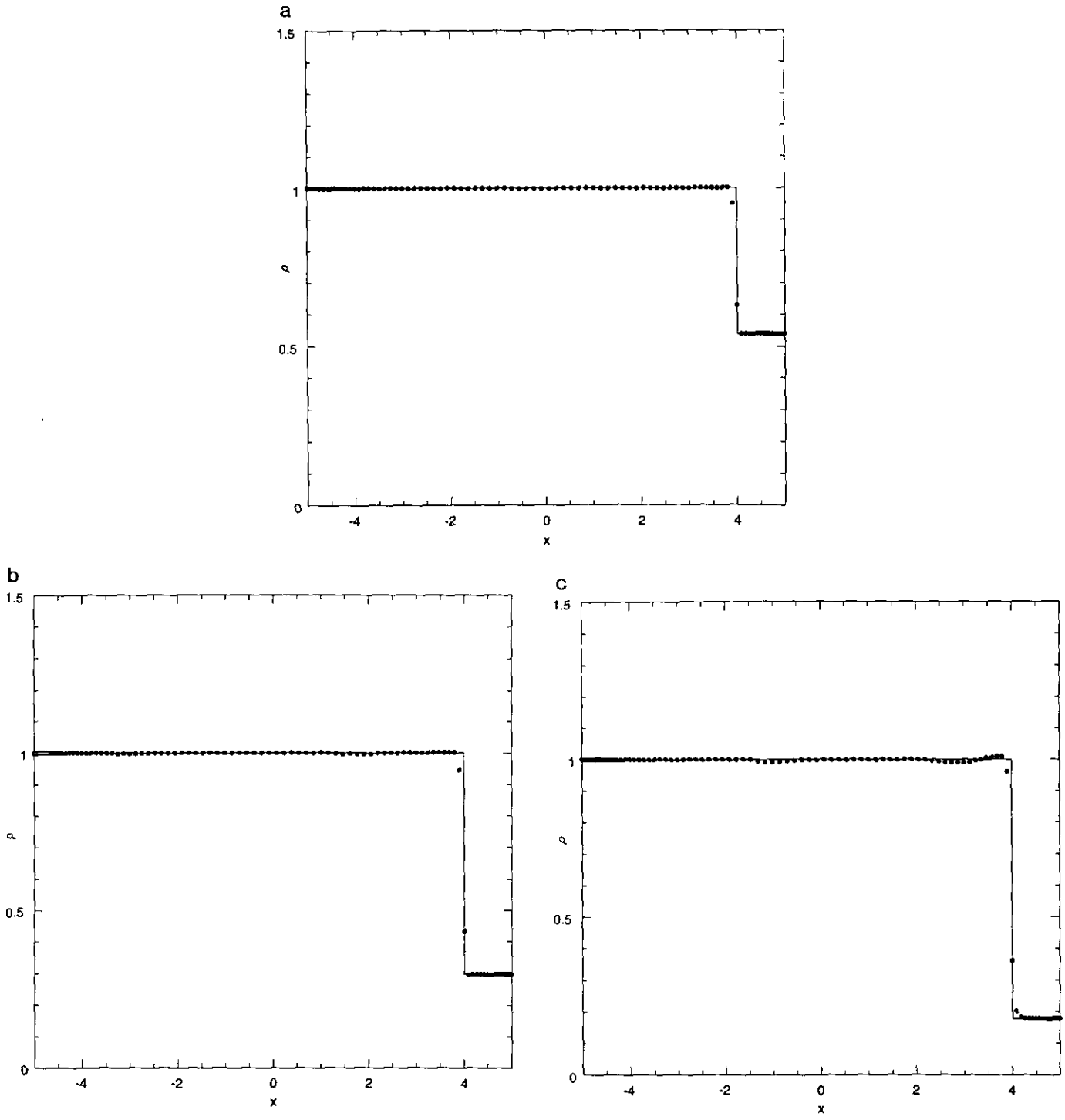

FIG. 13. Same as in Fig. 12 with the same number of mesh points. Now $K = 1$, $N = 101$. The moving shock is thus confined in the interior of a Chebyshev grid, where the variation of the mesh distance is only linear. Density profiles for the same incoming Mach numbers as in the previous figure.

strength in the Sod problem is $M_R^s = 1.656$ while the shock strength for the Lax problem is $M_R^s = 1.961$. For the single shock model problem presented above these values correspond to below and above the threshold M_L for the Sod and Lax problems, respectively. This is consistent with the fact that there exist post-shock oscillations in the Lax problem in multi-domains while the Sod problem is unaffected.

The results of the previous paragraph suggest that certain (K, N) discretizations can support stronger shocks than

others and that shocks of modest strength can be adequately resolved even in highly distorted meshes. This is true for more general shock tube problems where more than two phases are involved and thus complex interactions of shock waves with rarefaction fans and contact discontinuities occur. To demonstrate the robustness of the spectral element–FCT algorithm in such situations we solve the following two-diaphragm, three-phase problem:

$$\begin{aligned} &\rho_1 = 3.0, \quad u_1 = 0, \quad P_1 = 3.0, \quad -5 \leqslant x \leqslant -2, \\ &\rho_2 = 1.0, \quad u_2 = 0, \quad P_2 = 1.0, \quad -2 \leqslant x \leqslant 2, \\ &\rho_3 = 0.125, \quad u_3 = 0, \quad P_3 = 0.1, \quad 2 \leqslant x \leqslant 5, \end{aligned} \tag{25}$$

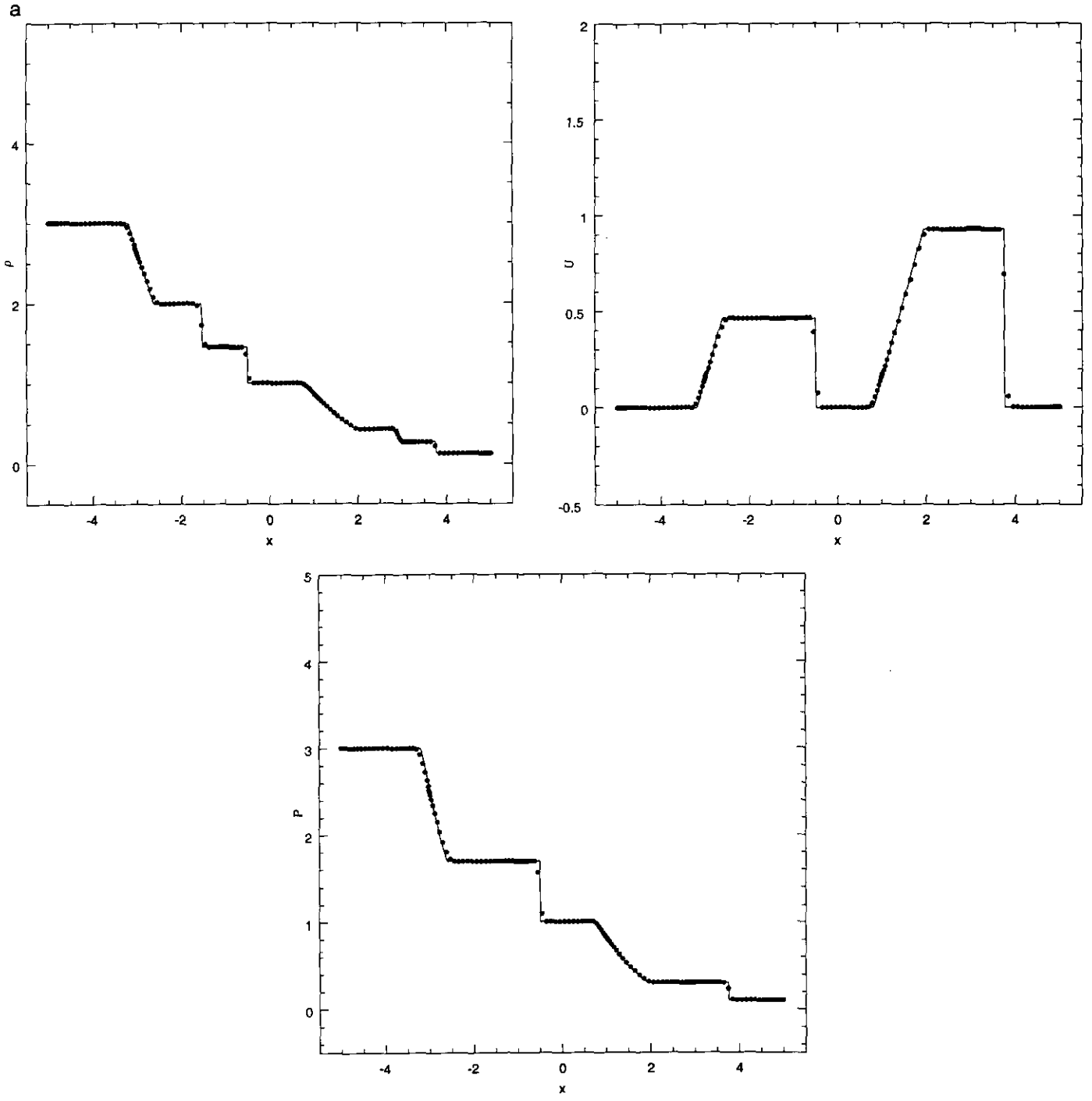

FIG. 14. Spectral element-FCT method. Solution of a shock-tube problem with two diaphragms and three phases. Discretization: $K = 5$, $N = 31$. Times (a) $t = 1.00$, (b) $t = 1.68$. Generation of moderate strength shocks, and interaction of simple waves. Profiles for density, velocity, pressure in (a), (b), (c), respectively.

for $t < 0$. The diaphragms are removed simultaneously at $t = 0$.

The spectral element–FCT ($K = 5$; $N = 31$) solution is plotted in Figs. 14a and 14b at times $t = 1.0$ and $t = 1.68$, respectively. The solid line represents a solution obtained with an eight-order finite difference–FCT scheme on a uniform mesh with 1000 points. The corresponding solutions (not shown here) with a second- and eighth-order finite difference–FCT scheme produce smearing and terracing of the solution both at the early instant ($t = 1.0$), where the shock propagating to the right crosses an expansion fan propagating to the left as well as at the late instant.

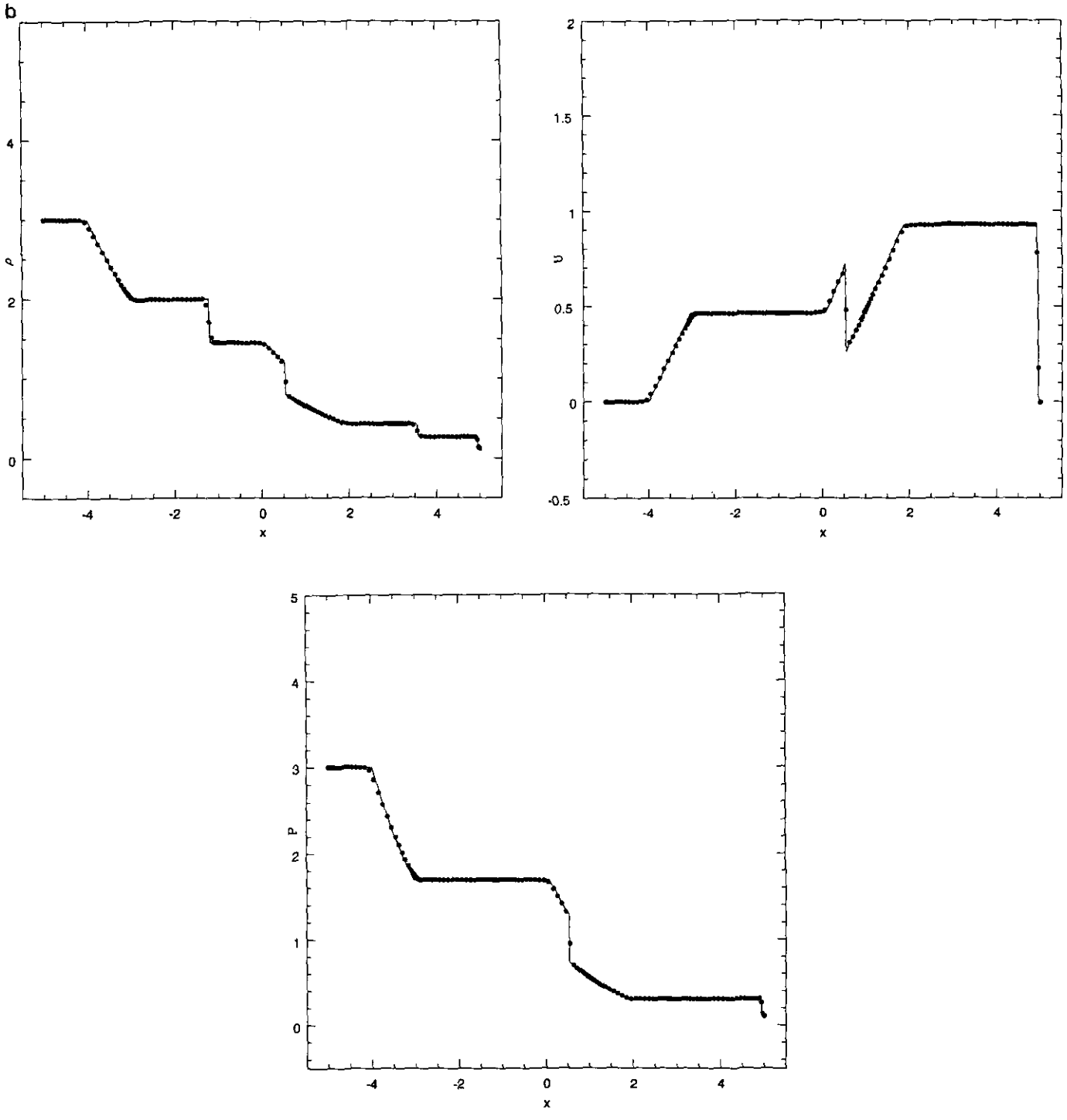

FIGURE 14—*Continued*

3. TWO-DIMENSIONAL FORMULATION

3.1. *Euler Equations in Conservative Form*

The system of Euler equations for polytropic gas in two dimensions is given by

$$\mathbf{u}_t + \mathbf{f}(\mathbf{u})_x + \mathbf{g}(\mathbf{u})_y = 0 \tag{26}$$

with

$$\mathbf{u} = \begin{pmatrix} \rho \\ m \\ n \\ E \end{pmatrix}, \qquad \mathbf{f} = \begin{pmatrix} m \\ m^2/\rho + P \\ mn/\rho \\ (P+E)\, m/\rho \end{pmatrix}, \qquad \mathbf{g} = \begin{pmatrix} n \\ mn/\rho \\ n^2/\rho + P \\ (P+E)\, n/\rho \end{pmatrix}, \tag{27}$$

where $m = \rho u$, $n = \rho v$, and $P = (\gamma - 1)(E - \frac{1}{2}(m^2 + n^2)/\rho)$.

To construct the cell averages in two dimensions we first integrate Eq. (26) in x, i.e., $\int_{x_i-}^{x_i+}$, and subsequently in y, similarly from y_{i-} to y_{i+}. The final *conservative* form of the system on a *rectangular* two-dimensional mesh is

$$\frac{\partial}{\partial t}\overline{\overline{\mathbf{u}}}_{i,j} + \frac{\overline{\mathbf{f}_{i+,j}}^{y} - \overline{\mathbf{f}_{i-,j}}^{y}}{\Delta x_i} + \frac{\overline{\mathbf{g}_{i,j+}}^{x} - \overline{\mathbf{g}_{i,j-}}^{x}}{\Delta y_j} = \mathbf{0}, \tag{28}$$

where we have defined

$$\overline{\mathbf{f}_{i\pm,j}}^{y} = \frac{1}{\Delta y_j}\int_{y_j-}^{y_j+} \mathbf{f}(\mathbf{u}(x_{i\pm}, y))\, dy \tag{29a}$$

$$\overline{\mathbf{g}_{i,j\pm}}^{x} = \frac{1}{\Delta x_i}\int_{x_i-}^{x_i+} \mathbf{g}(\mathbf{u}(x, y_{j\pm}))\, dx \tag{29b}$$

$$\overline{\overline{u}}_{i,j} = \frac{1}{\Delta x_i}\frac{1}{\Delta y_j}\int_{y_j-}^{y_j+}\int_{x_i-}^{x_i+} u(x, y)\, dx\, dy. \tag{29c}$$

Here, the average quantities are evaluated at the Gauss points (i, j), while the one-dimensional-average quantities are evaluated at a mixed set of Gauss and Gauss–Lobatto poins (see Fig. 15 for nomenclature). De-averaging of the state vector $\bar{\bar{\mathbf{u}}}$ is obtained by successive application of the one-dimensional reconstruction procedure described in Section 2.4.

3.2. *Boundary and Interfacial Conditions*

As in the one-dimensional case, upon completion of every algorithmic cycle the reconstruction process produces states at the common flux-points of neighboring elements that are generally distinct. For instance in Fig. 15, at the point Q_1 of element e^1 reconstruction gives the state vector $\mathbf{u}^1$, whereas at the adjacent point Q_2 of element e^2 reconstruction gives

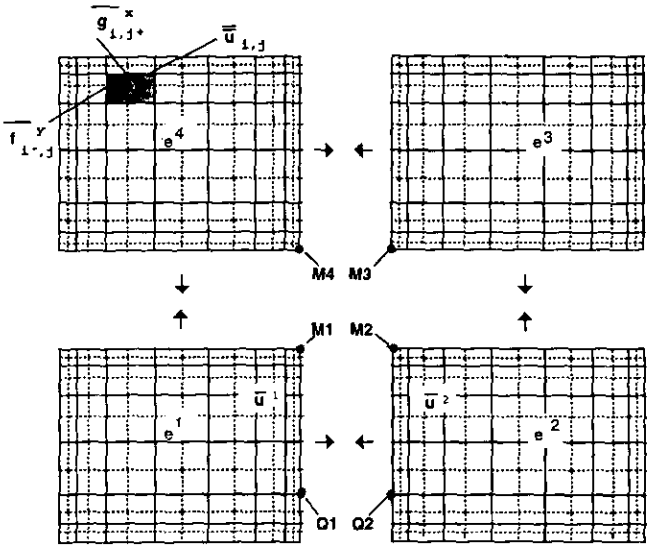

FIG. 15. Spectral element mesh and patching in two dimensions.

the state $\mathbf{u}^2$, generally different from $\mathbf{u}^1$. To take this into account we proceed as follows:

- We solve a one-dimensional Riemann problem for the states $\mathbf{u}^1$, $\mathbf{u}^2$. An approximate solver is used based on the Lax–Friedrichs scheme [33] or the modified Roe scheme [15].
- We assign the resulting fluxes to both points Q_1, Q_2; these fluxes will enter the flux-averaging algorithm on the interface.

The above procedure needs to be modified for the corner points at intersections of three or more elements. To this end, we observe that in the time-stepping we only use one-dimensional-average fluxes and not the fluxes themselves. With this in mind, we construct the following scheme for the corner points:

- Based on $\mathbf{u}^1$, $\mathbf{u}^2$ we solve a one-dimensional Riemann problem for $M_1 \equiv M_2$. The resulting fluxes are assigned to both M_1, M_2 and enter the averaging algorithm along the common boundary of e^1, e^2.
- Based on $\mathbf{u}^3$, $\mathbf{u}^4$ we solve a one-dimensional Riemann problem for $M_3 \equiv M_4$. The resulting fluxes are assigned to both M_3, M_4 and enter the averaging algorithm along the common boundary of e^3, e^4.

The same process will be repeated on these points for a second time to evaluate the fluxes along the other coordinate direction.

In supersonic inflow–outflow boundaries we follow the same scheme, with any given state being regarded as coming from reconstruction on a fictitious element. This automatically ensures compatibility with the physics of the problem. In the case of reflecting boundaries, we again solve a one-

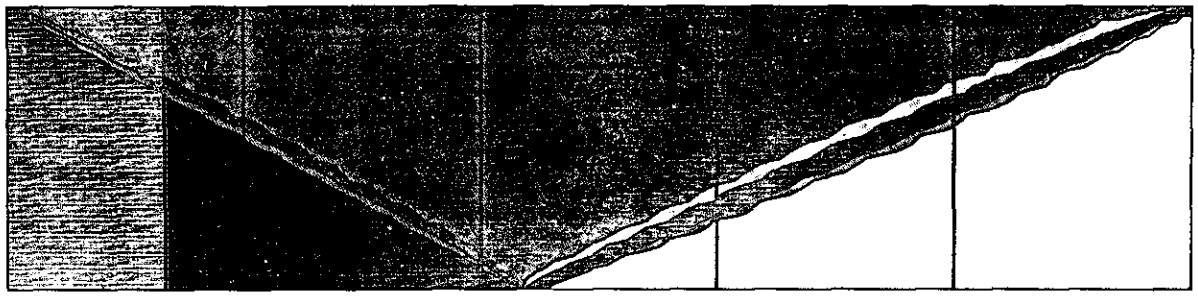

FIG. 16. Two-dimensional Euler equations solved with spectral element-FCT method. Shock reflection on a flat plate. Mach number of the incoming flow is 2.9. Density profile (10 contours on a 5-element mesh).

dimension Riemann problem, by creating a mirror image of the reconstructed state $\mathbf{u}$. This fictitious state has a reversed sign in the conservative variable containing the velocity normal to the boundary.

3.3. *FCT Method*

The spectral element–FCT method in two dimensions is very similar to the one described in Section 2.2 for one-dimensional flows. The main steps of the proposed algorithm are as follows:

- Step 1. Evaluate the field of cell averages corresponding to the initial condition.
- Step 2. Compute the transportive fluxes corresponding to the low-order scheme. The low-order positive-type scheme used here is either the Lax–Friedrichs scheme or the modified Roe scheme. The low-order fluxes are denoted by $\mathbf{F}$ and $\mathbf{G}$ in x- and y-directions, respectively.
- Step 3. Advance (explicitly) cell averages in time using low-order fluxes to obtain the low-order transported and diffusive solution $\bar{\mathbf{u}}$. This is done using the third-order Adams–Bashforth scheme or a hybrid Euler–forward/Adams–Bashforth time-stepping scheme as was discussed in Section 2.3.
- Step 4. Compute the transportive fluxes $\mathbf{f}$ and $\mathbf{g}$ corresponding to the spectral element discretization at the Gauss–Lobatto points and perform one-dimensional averaging to obtain the fluxes $\bar{\mathbf{f}}^y$ and $\bar{\mathbf{g}}^x$ to be used in Step 5 (instead of $\mathbf{f}$, $\mathbf{g}$).
- Step 5. Compute the antidiffusive fluxes $\mathbf{Af} = \mathbf{f} - \mathbf{F}$ and $\mathbf{Ag} = \mathbf{g} - \mathbf{G}$.
- Step 6a. Limit $\mathbf{Af}$ (characteristic-wise) based on the transportive–diffusive field $\bar{\mathbf{u}}^{td}$ and advance in time (using an Adams–Bashforth third-order or the hybrid scheme) to obtain an intermediate state $\tilde{\bar{\mathbf{u}}}$.
- Step 6b. Limit $\mathbf{Ag}$ (characteristic-wise) based on the intermediate field $\tilde{\bar{\mathbf{u}}}$ and advance in time (using an Adams–Bashforth third-order or the hybrid scheme) to obtain the final field at time level $(n+1)$.
- Step 7. Reconstruct point values from the cell averages at the new time level.
- Step 8. If the target time is not achieved go to Step 2.

3.4. *Numerical Results*

Next, we present two-dimensional examples: The first problem involves an oblique shock reflected from a solid wall. The computational domain is rectangular extending from $0 \leqslant x \leqslant 4.12829$ and $0 \leqslant y \leqslant 1$ and discretized with $K = 5$ and 10 elements, with 21 points in each direction. The initial conditions correspond to $\rho = 1.0$, $u = 2.9$, $v = 0.0$, and $P = 1/1.4$ throughout the domain. The boundary conditions

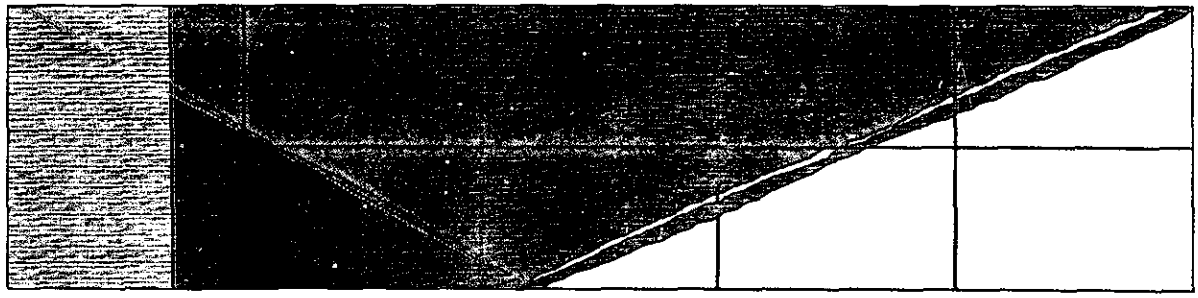

FIG. 17. Two-dimensional Euler equations solved with spectral element-FCT method. Shock reflection on a flat plate. Mach number of the incoming flow is 2.9. Density profile (10 contours on a 10-element mesh).

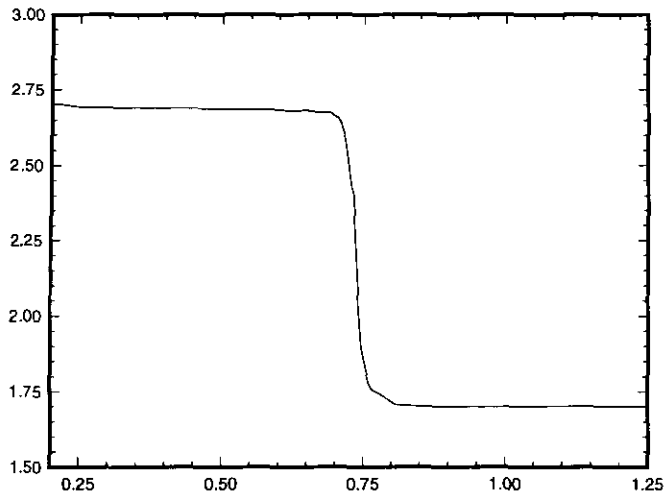

FIG. 18. *Density profile normal to the reflected shock (10 element mesh).*

applied are: inflow boundary condition at $x = 0$ and outflow boundary conditions at $x = 4.12829$. At the upper boundary the post-shock condition is prescribed ($\rho = 1.7$; $u = 2.61932$; $v = -0.506339$; $P = 1.52824$). At the lower boundary ($y = 0$) a reflection boundary condition is imposed. The exact solution to this problem is an incoming shock of 29° with the lower boundary and a reflected shock of 23.28°. The exact solution past the second shock is described by ($\rho = 2.68732$; $u = 2.40148$; $v = 0$; $P = 2.93413$). In Fig. 16 we show a contour plot with 10 density levels for the solution on the five-element mesh. The solution on the ten-element mesh appears on Fig. 17; the improvement in accuracy due to refinement is obvious. In both cases, the essential geometrical features of the flow field are reproduced accurately. The angle of the reflected shock is indeed 23° and the pressure ratio at a point in the middle of the region past the second shock ($x = 3.5$, $y = 0.31$) is $P = 2.9376$ which represents a deviation of 0.12% with respect to the exact value. Taking a density profile in a direction normal to (and approximately halfway along) the second shock no oscillations around the transition region (Fig. 18).

The second two-dimensional simulation is the interaction of a shock with an expansion fan. A Mach 2.9 diatomic ideal gas flow generates a shock at a compression corner of 16°; the downstream flow expands around a second corner that restores the original flow direction. The corresponding spectral element discretization consists of 12 element of variable size with 20×20 collocation points in each element (see Fig. 19). The lower boundary corresponds to an inviscid wall and the upper as well as the exit are supersonic outflows. The initial conditions correspond to a Mach 2.9 flow everywhere. The computed density distribution is shown in Fig. 20 at time $t = 16$. The geometrical features reproduced here are the correct ones [41]. For example, the shock propagates at 34° angle, in agreement with gas tables while the expansion fan meets the shock at the correct location as computed by the corresponding iso-Machs (not shown here). There are no visible differences in the slopes of density contours across elemental interfaces; this validates the implementation of the interface conditions presented in this work.

The last example we present is a two-dimensional simulation of supersonic flow over a forward-facing step, a standard benchmark test in the literature (see [42]). The domain extends from $x = 0$ to $x = 3$ and from $y = 0$ to $y = 1$ with the origin located at the lower leftmost corner. Discretization is made with 252 elements of 5×5 collocation

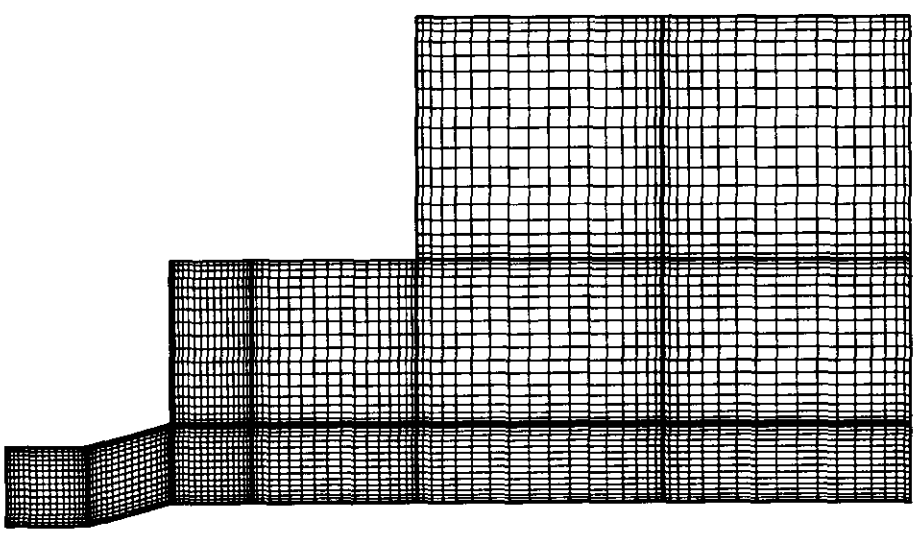

FIG. 19. Spectral element mesh for the compression ramp/expansion corner problem.

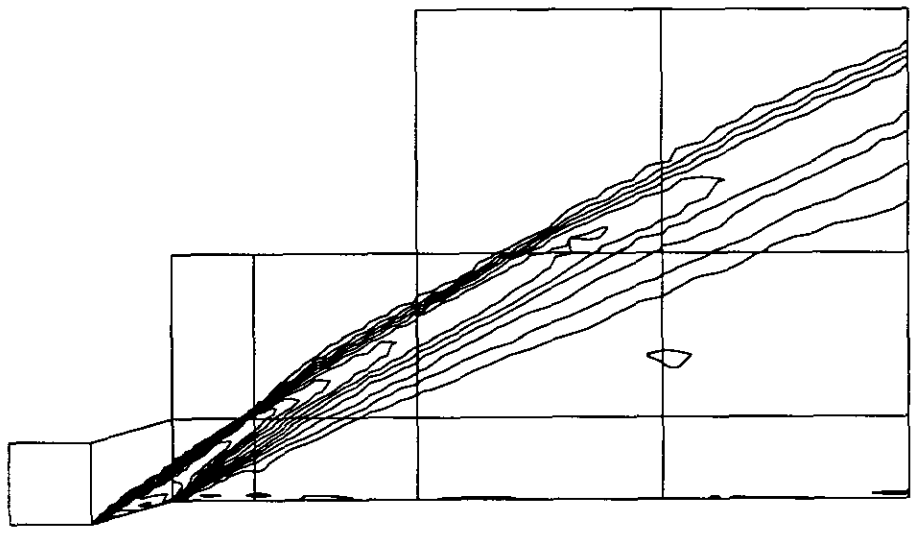

FIG. 20. Simulation of a Mach 2.9 flow impiging a compression ramp/expansion corner configuration. The shock emanating from the ramp interacts with the expansions fans around the corner.

points each; the corresponding spectral element mesh is shown in Fig. 21. This resolution is equivalent to the medium resolution (40×120) employed in [42]. The initial conditions as well as the boundary conditions at the inflow at $x = 0$ are $\rho = 1.4$, $u = 3.0$, $v = 0.0$, and $P = 1$ throughout the domain, which corresponds to a Mach-3 flow. The rest of the boundary conditions are: supersonic outflow at $x = 3$ and reflection boundary conditions along both the bottom and the top of the domain. A hybrid time-stepping algorithm consisting of an Euler–forward/Adams–Bashforth third-order scheme (as described in Section 2.3) was employed for the temporal discretization.

In Fig. 22a we plot density contours with 30 levels at time $t = 2.5$. The agreement with the high resolution run of Woodward and Collela [42, p. 13] is excellent: the step on the upper wall has been formed and it has the right length while the reflected shock passes exactly through the upper corner at the exit of the domain. In addition, the contact discontinuity in the upper wall as well as the reflection due to the step corner shock and its subsequent propagation across the domain are in close agreement with the high resolution results of Woodward and Collela and the more recent results of Casper obtained with a high-order ENO scheme [5]. The same is also true for the density field at time $t = 4.0$ (Fig. 22b); here, however, the appearance of a Mach stem in the lower wall alters the results slightly. Treatment of the singularity at the step corner following the approach of Collela and Woodward reduces that artificial stem but it does not completely eliminate it; this result was also obtained using the ETBFCT method by Woodward and Collela [42, p. 151]. Unlike the ETBFCT results, however, for the pressure field, in our calculations the preshock region is not influenced by the shock and the pressure remains always positive. Also, the staircase effect present in the ETBFCT calculation with the medium resolution mesh is largely absent in our calculation.

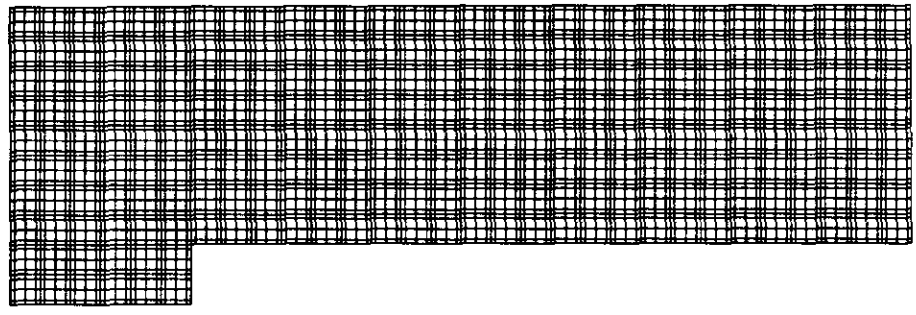

FIG. 21. The spectral-element mesh for the Mach 3 flow over a forward-facing step. $K = 252$, $N = 5$.

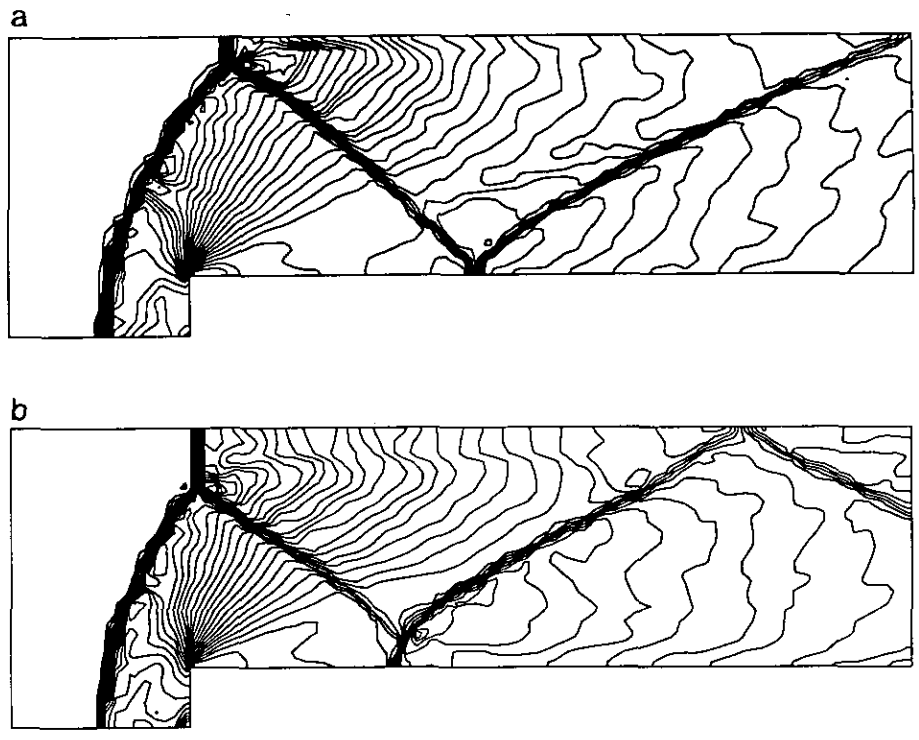

FIG. 22. Results of the two-dimensional spectral element-FCT code for the Mach 3 flow over a forward facing step. Density profiles with 30 contours on each. Times (a) $t = 2.5$, (b) $t = 4.0$.

4. DISCUSSION

In this work, we have extended the spectral element–FCT method to systems of hyperbolic conservation laws in one and two dimensions. While monotonicity in the current algorithm is ensured by employing the standard FCT limiters of Boris and Book, the conservative property is guaranteed by the discretization that employs a staggered grid of Gauss and Gauss–Lobatto Chebyshev collocation points. In this setting, fluxes are computed at the Gauss–Lobatto points while cell averages are computed at the Gauss points (the "cell midpoints" in the spectral Chebyshev space).

As regards time discretization, it was found that a hybrid time-stepping scheme, that activates an Euler forward algorithm around the discontinuities and an Adams Bashforth scheme of third order in the smooth part of the domain, privides the most accurate results. In particular, it eliminates the previously observed terracing effects in smooth waveforms as it reduces significantly the dispersion errors; the terracing effect was shown to be strongly dependent on the phase properties (see also [11]). To this end, many attempts have been made in the past to increase the accuracy in phase properties of finite difference/volume FCT methods [28]; this property is provided naturally in the proposed algorithm by the spectral representation. It was also shown for one-dimensional model problems that the resolution of contact discontinuities scales with the formal order of accuracy of the scheme, in agreement with the theory of Harten [14] and the subsequent findings of Roe [36]. In two dimensions, we have demonstrated the accuracy of the spectral element–FCT method by comparing with two benchmark solutions as well as the flexibility in handling non-rectangular domains using multi-element decomposition. This discretization is similar to the $h-p$ discretization of Oden [6] and provides great flexibility since a variable number of macro-elements or collocation points per element can be employed to accomodate both accuracy and geometric requirements.

The computational complexity of the method is similar to standard ENO algorithms of the same degree of approximation; the main cost is encountered in reconstruction and scales (in two-dimensions) as KN^3, where K is the number of elements and N is the number of collocation points per direction. Fast Chebyshev transforms can be employed for large values of N to reduce this cost. As regards time step restrictions due to the clustering of collocation points at elemental boundaries, the use of low-order (relatively low N) elements alleviates this constraint; for large values of N a transformation method similar to that of [24] would seem to be appropriate, given also the experience in [7] but it has not yet been implemented in our code.

A difficulty we encountered in shock-tube problems is associated with the low-order scheme employed in the FCT

algorithm. By this, we refer to the appearance of occasional $O(1)$ errors behind a moving strong shock which we studied systematically in the first part of this paper; this problem is typical of shock-capturing methods on non-uniform meshes if the collocation points cluster or expand superlinearly [37, 34]. These post-shock oscillations did not appear in the two-dimensional examples reported here, either because the shocks were not sufficiently strong or strong shocks were not moving through the elements.

ACKNOWLEDGMENTS

We thank Dr. D. Sidilkover for his help with some of the subroutines used in this work and Professors D. Gottlieb and C. W. Shu of Brown University for many helpful suggestions. This work was supported by AFOSR Grant 90-0261 and by NSF Grant ECS-90-23760.

REFERENCES

1. J. P. Boris and D. L. Book, *J. Comput. Phys.* **11**, 38 (1973).
2. W. Cai, Gottlieb, and A. Harten, Report No. 90-72, ICASE, 1990 (unpublished).
3. W. Cai, D. Gottlieb, and C. W. Shu, *Math. Comput.* **52**, 389 (1989).
4. W. Cai and C. W. Shu, *J. Comput. Phys.* **104**, 427 (1993).
5. J. Casper, Ph.D. thesis, Old Dominion University, 1990.
6. L. Demkowicz, J. T. Oden, and W. Rachowicz, *Comput. Methods Appl. Mech. Eng.* **84**, 275 (1990).
7. W. S. Don, *J. Comput. Phys.*, **110**, 103 (1994).
8. W. S. Don and D. Gottlieb, *Comput. Methods Appl. Mech. Eng.* **80**, 39 (1990).
9. C. W. Gear, *Numerical Initial Value Problems in Ordinary Differential Equations* (Prentice–Hall, Englewood Cliffs, NJ, 1973).
10. J. Giannakouros, Ph.D. thesis, Princeton University, 1994.
11. J. Giannakouros and G. E. Karniadakis, *Int. J. Numer. Methods Fluids* **14**, 707 (1992).
12. S. K. Godunov, *Mat. Sb.* **47**, 271 (1959).
13. N. Grandzouan, *J. Comput. Phys.* **91**, 424 (1990).
14. A. Harten, AEC Research and Development Report C00-3077-50 (New York University, New York, 1974).
15. A. Harten and J. M. Hyman, *J. Comput. Phys.* **50**, 235 (1983).
16. A. Harten, P. D. Lax, and B. Van Leer, *SIAM Rev.* **25** (1), 35 (1983).
17. A. Harten and G. Zwas, *J. Comput. Phys.* **9**, 568 (1972).
18. S. M. O. Kaber, Ph.D. thesis, Université Pierre et Marie Curie, Paris, 1992.
19. G. E. Karniadakis, *Appl. Numer. Math.* **6**, 85 (1989).
20. G. E. Karniadakis, E. T. Bullister, and A. T. Patera, "A Spectral Element Method for Solution of Two- and Three-Dimensional Time Dependent Navier–Stokes Equations," in *Finite Element Methods for Nonlinear Problems* (Springer-Verlag, New York/Berlin, 1985), p. 803.
21. D. A. Kopriva, AIAA Paper 93-3376.
22. D. A. Kopriva, *J. Comput. Phys.* **96**, 428 (1991).
23. D. A. Kopriva, Report No. FSU-SCRI-93-17, Supercomputer Computations Research Institute, Florida State University, 1993; *J. Comput. Phys.*, submitted.
24. D. Kosloff and H. Tal-Ezer, Report No. 89-71, ICASE, 1989 (unpublished).
25. P. D. Lax, "Accuracy and Resolution in the Computation of Solutions of Linear and Nonlinear Equations," in *Recent Advances in Numerical Analysis, Proc. Symp. Math. Research Center, University of Wisconsin* (Academic Press, New York/London, 1978), p. 107.
26. B. Van Leer, *J. Comput. Phys.* **32**, 101 (1979).
27. B. E. McDonald, *J. Comput. Phys.* **82**, 413 (1989).
28. D. Odstrčil, *J. Comput. Phys.* **91**, 71 (1990).
29. E. S. Oran and J. P. Boris, *Numerical Simulation of Reacting Flows* (Elsevier, Amsterdam/New York, 1987).
30. S. Osher and F. Solomon, *Math. Comput.* **38**, 339 (1982).
31. A. T. Patera, *J. Comput. Phys.* **54**, 468 (1984).
32. D. Pathria and G. E. Karniadakis, *J. Comput. Phys.*, submitted.
33. P. J. Roache, *Computational Fluid Dynamics* (Hermosa, Albuquerque, NM, 1982).
34. P. L. Roe, private communication.
35. P. L. Roe, *J. Comput. Phys.* **43**, 357 (1981).
36. P. L. Roe and M. J. Baines, "Algorithms for Advection and Shock Problems," in *Notes on Numerical Fluid Dynamics (Proceedings of the Fourth GAMM-Conference on Numerical Methods in Fluid Mechanics*, edited by H. Viviand (Vieweg, Braunschweig, 1982), p. 281.
37. C.-W. Shu, private communication.
38. D. Sidilkover and G. E. Karniadakis, *J. Comput. Phys.* **107**, 10 (1993).
39. G. A. Sod, *J. Comput. Phys.* **27**, 1 (1978).
40. G. A. Sod, *Numerical Methods in Fluid Dynamics* (Cambridge Univ. Press, Cambridge, UK, 1985).
41. P. A. Thompson, *Compressible-Fluid Dynamics* (McGraw–Hill, New York, 1988).
42. P. Woodward and P. Collela, *J. Comput. Phys.* **54**, 115 (1984).
43. S. T. Zalesak, *J. Comput. Phys.* **31**, 335 (1979).
44. S. T. Zalesak, "A Physical Interpretation of the Richtmyer Two-Step Lax–Wendroff Scheme, and Its Generalization to Higher Spatial Order," in *Advances in Computer Methods for Partial Differential Equations, V*, pages 491–496, 1984.